Materials Characterization 172 (2021) 110884

Contents lists available at ScienceDirect

Materials Characterization

journal homepage: www.elsevier.com/locate/matchar

Electromagnetic-wave shielding promulgation of cluster like FZ@MWCNT composite incorporated in GO matrices by polarization relaxation and potential degradation

Chandi Charan Dey [a], Ayan Mallick [a], Abhik Sinha Mahapatra [b], Madhumita Dalal [a], Pabitra Kumar Chakrabarti [a,*]

[a] Solid State Research Laboratory, Department of Physics, Burdwan University, Burdwan 713104, West Bengal, India
[b] Department of Physics, JIS University, Kolkata 700109, West Bengal, India

ARTICLE INFO

Keywords:
MWCNTs
Graphene oxide
Magnetic properties
Dielectric losses
Microwave absorption

ABSTRACT

To protect against the adverse effects of electromagnetic (EM) radiation in the range of radio- to micro-waves, we have developed new polymer-based nanocomposites consisting of high dielectric, magnetic, and conducting columns. We have optimized the synthesis of γ-Fe_2O_3 and ZnO in different potential matrices such as multiwall carbon nanotubes (MWCNT) and graphene oxide (GO), termed as FZ@MWCNT and FZ@MWCNT-GO. Saturation magnetization, coercive field and MT curve suggest the mixture of superparamagnetic and ferrimagnetic nanoparticles blocked at room temperature. The electromagnetic attenuation of these composites containing 60 wt% with paraffin wax shows a significant improvement in the maximum shielding efficiency of 56.7 dB, making FZ@MWCNT and FZ@MWCNT-GO very good candidates for electromagnetic shielding. In addition, the extraordinary enhancement of absorption is attributed to the synergistic effect of dielectric losses due to conductivity, interfacial polarization as well as magnetic losses due to magnetic resonances and eddy current impact.

1. Introduction

Now-a-days the artificial intelligence which is the driving factor behind the next generation of scientific and technological developments is considered as the most strategic high-tech future. The explosive growth of the intelligent era is inextricable from the advancement of various electronic and electrical smart devices, especially with the coming 5G era [1–3]. But the harmful effects of radiations in the range of radio and microwaves emitted from different essential electronic components of communication devices are a burning issue in today's and tomorrow's society. People and electronic devices are not safe for the rapid use of microwave devices in all parts of society [4,5]. Low-dimensional EM functional material with electromagnetic interference (EMI) shielding devices are widely desirable to be protected from the ill effects of microwaves [6]. Due to this rapid expansion of science and technology, the EMI affects the water bodies and also creates air pollution [7,8]. From the human perspective, the adverse effect of EMI is surprisingly profound because it can demolish DNA, weaken the biological immune system, and extensively threaten social health [9]. Besides, microwaves are universally used for detection, navigation, and air communications in the defense system. In current research, there is now a challenge to protect humans, as well as others mentioned above from the ill effect of EMI [10]. Most research in this area is looking for a practical and cost-effective EMI shielding material that can safely protect against all adverse effects in society. To overcome these microwave risks and to protect living and non-living entities, it is necessary to design and fabricate shielding devices. For a good microwave shielding material, it must be physically and chemically stable, have low specific gravity, high absorption, flexibility, a large absorption frequency range, better conductivity, easy implementation, and an economic cost [11]. Since low reflection loss indicates efficient energy conversion and heat production, high electromagnetic absorption allows the material extremely useable on multifunctional electromagnetic nano-micro devices [12]. Conventional applications of metal plates as shielding materials are fundamentally dependent on reflection, not on absorption, which reduces with increasing frequency [10]. The difficulty of application of the metallic system as EMI shielding is limited due to low corrosion resistance, heavy processing, heavy-weight, secondary pollution, high risk of oxidation, and also it needs

---

* Corresponding author.
E-mail address: pabitra_c@hotmail.com (P.K. Chakrabarti).

https://doi.org/10.1016/j.matchar.2021.110884
Received 15 October 2020; Received in revised form 30 December 2020; Accepted 4 January 2021

surface modification. An EM wave absorber is, in general, a functional material that minimizes the reflection and transmission of microwaves and absorbs it dramatically by converting wave energy into thermal energy [13]. In many cases, carbonaceous nanomaterials blended with polymer promptly overcome metal performance deficiencies [14].

Zhu et al. [15] synthesized the porous Fe_3O_4 sphere anchored on the CNT matrix by the solvothermal method, which developed the 3D network connecting nanoparticles with CNT and in this case the microwave absorption is quite good (−51 dB) where the bandwidth is also high. Large surface areas and the porous formation of Fe_3O_4 magnetite nanoparticles and controllable permittivity are responsible for this good synergetic performance in microwave absorption. Jian et al. [16] reported an easy synthesis method to fabricate nanoscale Fe_3O_4/graphene capsules (GCs) by catalytic chemical vapor deposition and hydrothermal process. The unique morphology contributes to a better synergy among Fe_3O_4 particles and GCs to boost microwave absorption (−32 dB). The best performance is based on the reasonable impedance matching, the occurrence of the interface, and the polarization of free carriers. Wang et al. demonstrated a chemoselective route to induce Fe_3O_4@ZnO core-shell nanoparticles decorating carbon nanotube to build MWCNT/Fe_3O_4@ZnO heterotrimers with a moderate reflection loss value of −40.9 dB [17]. Singh et al. [18] prepared Fe_3O_4 nanoparticles (15 nm) infiltrated vertically aligned MWCNT sandwiched with rGO sheets network for high-performance EMI shielding (−37 dB). Hekmatara et al. [19] concluded that the combination of magnetite (Fe_3O_4) with MWCNT influences the electric field component of the microwave that may help the attenuation of wave along with other causes. Tsonos et al. analyzed the parallel investigation of Fe_3O_4/MWCNT and Fe_3O_4/graphene nanoparticles in the PVDF matrix [20]. Guo et al. [21] noted that polypyrrole coated Fe_3O_4 also improved the EM wave absorption due to increased surface area, eddy current impact, and anisotropy strength.

From the previous discussion, it is noteworthy that composite of γ-Fe_2O_3 and ZnO including CNT or GO upgrade the microwave absorption in comparison with pristine γ-Fe_2O_3 counterpart due to the synergistic influence of dielectric and magnetic loss, impedance matching, multiple reflection, and various polarization. According to our perception, there is hardly any report concerning the EMI shielding effectiveness of γ-Fe_2O_3 and ZnO composite with MWCNT and GO matrix prepared by the co-precipitation approach. These composite may have higher magnetic and dielectric losses and may exhibit enhanced interfacial polarization as well as dielectric relaxation. Since EM waves have both electric and magnetic vector fields, these composite materials, including dielectric and magnetic materials, deliver a significant reservation for dielectric and magnetic losses. Magnetic materials will contribute to the aforementioned loss mechanisms by magnetic resonance or eddy current effect [22], and dielectric materials serve the similar by polarization or conductivity loss. Among the family of microwave absorber materials, maghemite is well suited for materials with magnetic loss and unusual magnetic permeability, moderate expense, non-toxicity, and environmental benignity [23]. However, poor impedance matching, limited conductivity, inefficient dielectric loss, and narrow absorption bandwidth limit its subsequent application [24]. Although there are some limitations of MWCNT and GO such as agglomeration and accumulating nature due to Van der Waal forces, we still consider it due to its high aspect ratios, impedance matching, conductivity, high absorption bandwidth, dielectric property, lightweight, thermal stability and skin depth [25,26]. Also the reflection, transmission and absorption of microwaves can be monitored by using the large active surface areas of graphene electrodes [27]. GO and MWCNTs are the most promising for impedance matching, broadening of absorption bandwidth whereas performance of dielectric ZnO, and magnetic maghemite nanoparticles easily recover the dielectric and magnetic losses. In the present study, we propose a very simple, highly effective and inexpensive non-conventional route to avoid agglomeration of nanoparticles: MWCNTs including GO are dispersed in a polymer mold such as paraffin wax while nanoparticles are further intercalated on the surface. It can be seen here that the composites of maghemite, ZnO and GO incorporated separately in MWCNT are promising microwave absorbers.

2. Synthesis of γ-Fe_2O_3-ZnO composite with GO and MWCNT

A two-step procedure is followed to prepare a mixture of γ-Fe_2O_3 and ZnO. During the preparation of γ-Fe_2O_3 through conventional chemical route it has been found in many cases that along with the desired phase some other impurity phases, the most common was α-Fe_2O_3, also get developed [28,29]. To avoid this fact in the present case we have considered an unconventional technique for the preparation of maghemite nanoparticles via the preparation of magnetite particles following the next reaction [30]

$$2\ Fe^{3+}_{(ac)} + Fe^{2+}_{(ac)} + 8\ OH^{-} \rightarrow Fe_3O_{4(\downarrow)} + 4\ H_2O_{(l)}$$

$$2\ Fe_3O_{4(pp)} + \frac{1}{2}O_{2(g)} \xrightarrow{[H^+]} 3\ \gamma - Fe_2O_{3(\downarrow)}$$

For this, $FeCl_3$ and $FeCl_2$ salt (2:1 mol) are chosen as precursor salts. Moreover, the solution of Fe^{+2} and Fe^{+3} is prepared by their aqueous suspension in triple-distilled water. After heating the solution at 50 °C for 15 min, the solution is then co-precipitated with an ammonia solution with constant stirring. Finally, the black color particles are precipitated, and those particles are thoroughly washed by distilled water with continuous mechanical stirring. The obtained precipitation changes its color from black to brownish black during washing. Then these obtained precipitation is separated and exhausted for slow evaporation at room temperature to obtain the desired nanoparticles.For the preparation of ZnO, the aqueous salt of ZnO is precipitated by adding an aqueous solution of NaOH drop-wise. The final pH is kept at ~10 and this condition is maintained for another 2 h under stirring to complete the reaction. The final product is then filtered and the precipitated hydroxide nanoparticles are thoroughly washed to isolate unwanted ions from the desired one. Finally, the filtered precipitate is annealed at 450 °C for 4 h to obtain ZnO nanoparticles.

The nanoparticles of ZnO and maghemite (1:1) are exposed in a xylene medium for ultrasonication for 1 h. In this medium MWCNT is slowly added under ultrasonication, keeping the weight ratio of γ-Fe_2O_3-ZnO to MWCNT as 9:1. Then ultrasonication continues for another 1 h and the xylene is slowly evaporated out from the mixture and the product sample γ-Fe_2O_3-ZnO @ MWCNT is designated as FZ@MWCNT. In the same procedure, maintaining the weight ratio of γ-Fe_2O_3-ZnO, MWCNT and GO to 9:0.5:0.5, nanocomposite of FZ@MWCNT-GO is prepared. Whereas GO is prepared by modified Hummer's method. Now for the cylindrical shape paraffin wax is melted at 55 °C and then composites with 60 wt% are taken to the melted matrix for well and uniform dispersion. The melted matrix is then taken to the cylindrical shape holder designed of outer diameter 3.5 mm and an inner diameter of 1.52 mm.

3. Experimental section

3.1. Characterization techniques used

XRD analysis of the bare and composite system was recorded by powder X-ray diffractometer, Model BRUKER D8 Advance with the Vinchi, using Cu Kα radiation (λ = 1.5405 Å). XRD patterns of the samples are analyzed by the Rietveld method using the MAUD program (version 2.33). For the morphological investigation TEM images were taken using a JEOL JEM 2100 HRTEM operating at 200 kV. Static magnetic properties were carried out using a VSM with maximum applied field of 5 T at different recording temperatures. Magnetization vs. temperature (M-T) curves were recorded under field cooled (FC) and zero field cooled (ZFC) conditions in the temperature range of 10–300 K. Electromagnetic shielding effectiveness was measured in different bands of microwave region using KEYSIGHTN5232B PNA-L network analyzer.

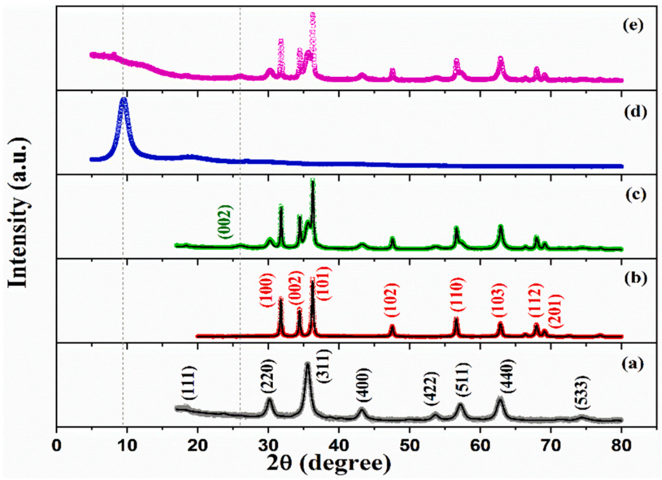

Fig. 1. XRD pattern of samples (a) γ-Fe_2O_3 (b) ZnO (c) FZ@MWCNT (d) GO (e) FZ@MWCNT-GO [Both the experimental and the generated pattern from Rietveld analysis are shown by dotted and continuous line].

3.2. XRD and Rietveld analysis

The XRD profiles of γ-Fe_2O_3, ZnO, FZ@MWCNT, GO and FZ@MWCNT-GO are shown in Fig. 1 respectively. Phase formation is further verified by analyzing the XRD profiles of γ-Fe_2O_3, ZnO and FZ@MWCNT using the Rietveld method (Figs. 1 a-c). The observed XRD patterns are simulated by repetitive refinement of various structural and microstructure parameters using space groups such as $P4_132$ and $P6_3mc$ in the case of γ-Fe_2O_3 and ZnO, respectively and both these two phases along with the hexagonal phase $P6_3/mmc$ in case of the nanocomposite, FZ@MWCNT. The goodness of fit is nearly 1 in each case (1.21, 1.60 and 1.83, respectively) implying pure phase formation in each sample. Based on the Popa model for size and r.m.s. lattice strain, the crystallite sizes of γ-Fe_2O_3 and ZnO are obtained as ~8 and 41 nm while r.m.s. lattice strains are 2.51×10^{-3} and 5.79×10^{-5}, respectively. According to the analysis, the atomic structure of γ-Fe_2O_3 contains three sites for the Fe^{3+} ions two of which are octahedral sites with atomic positions (0.875, 0.875, 0.875) and (0.125, 0.875, 0.125) and the third is the tetrahedral site with atomic position (0.5, 0.5, 0.5). In this atomic structure, O^{2-} ions are located at two sites with atomic positions (0.125, 0.142, 0.643) and (0.613, 0.613, 0.613). All these results, as well as the cell parameter of 8.3657 Å, confirm the pure phase formation of γ-Fe_2O_3 [31]. While the Zn^{+2} and O^{-2} ions are located at sites, (1/3, 2/3, 0) and (1/3, 2/3, 0.377) in ZnO, respectively with cell parameters a = b = 3.2496 and c = 5.2072 Å. XRD pattern of the nanocomposite, FZ@MWCNT is fitted considering three phases, $P4_132$, $P6_3mc$ and $P6_3/mmc$ simultaneously and without making any alteration in the atomic structures of γ-Fe_2O_3 and ZnO obtained from the refinement of individual profiles. XRD profile of the nanocomposite FZ@MWCNT was fitted accurately only when the three phases mentioned above are considered collectively. This fact confirms the coexistence of the three constituents, γ-Fe_2O_3, ZnO and MWCNT in the nanocomposite. The relative weight percentages of these three phases are 34, 52 and 14%, respectively which are close to the percentages of the three constituents taken during preparation of the nanocomposite.

3.3. TEM analysis

From the micrographs obtained for FZ@MWCNT displayed in Fig. 2 (a-c) and based on the size analysis performed in the previous section, larger nanoparticles are marked ZnO and smaller nanoparticles γ-Fe_2O_3 (Fig. 2a). The encapsulation of nanoparticles in MWCNT is authenticated from the micrographs (Fig. 2b), and also it is prominent that the nanoparticles are well dispersed throughout the complete matrix by a cluster pattern associated with the matrix. These kinds of cluster improvements occur through the π interaction within MWCNTs and nanoparticles. The nanoparticles are attached to the MWCNT's surface through this π interaction bond by magnetophoresis. Even by applying a strong magnetic field gradient, these nanoparticles cannot be separated from the conjugate materials [32]. Again MWCNTs are weakly diamagnetic i.e. they have a very light magnetic response; magnetic nanoparticles can be bound to MWCNTs. The crystal lattice spacing, calculated as 0.309 nm from Fig. 2d is ensuring (220) crystalline planes of γ-Fe_2O_3. Rings with different diameters of the SAED pattern (Fig. 2e) are assigned to different crystallographic planes viz. (100) [for ZnO], (311), (400), (220) [for γ-Fe_2O_3], (002) [for MWCNT] which confirms the presence of different components in the nanocomposite state. The corresponding lognormal fitting of histogram (Fig. 2f) shows that the average particle size is ~10 nm indicating that the nanoparticles observed in the micrograph are mainly crystallites of γ-Fe_2O_3. Finally to ensure the coexistence of γ-Fe_2O_3 and ZnO in the nanocomposite, EDAX analysis (Fig. 2 g) is performed which assures the presence of elements in the ratio which is quite consistent with the proposed composition ratio.

3.4. Static magnetic properties

The static magnetic properties of the γ-Fe_2O_3 sample and its composites are recorded in the temperature range from 10 K to 300 K. To study the response of magnetization to the magnetic field magnetic hysteresis loops are recorded at 10 K and 300 K, which are as presented in Fig. 3. From the figure, we observe that the magnetization of γ-Fe_2O_3 sample and its composites show a steady increase with the increase in the magnetic field up to ~1 T and beyond that magnetization increases slowly with the applied magnetic field. This increase continues until the maximum applied field of ~5 T even at 10 K. This type of variation confirms the presence of superparamagnetic (SPM) NP along with magnetically ordered state. The values of the coercive fields (H_C) extracted from the graph for the samples γ-Fe_2O_3, FZO, FZ@MWCNT, and FZ@MWCNT-GO are 7.5, 19.2, 6.7 and 4.2 Oe at 300 K and 198.8, 159.1, 167.6 and 315.1 Oe at 10 K, respectively. Such low value of H_C at RT also provides evidence of presence of SPM particles in the samples. The corresponding values of the saturation magnetization (M_S) are 66.2, 35.9, 29.5 and 34.7 emu/g at 300 K and 75.7, 42.2, 35.2 and 39.2 emu/g at 10 K, respectively. The observed value of M_S of γ-Fe_2O_3 at 10 K is about 90% of the saturation magnetization of the bulk ferrimagnetic maghemite (γ-Fe_2O_3) [33]. This decrease in the maximum magnetization value is due to the presence of fraction of SPM particles in the samples [34]. We also observed that the value of M_S at RT is much lower as compared to that at 10 K. This may be due to the shift of the SPM particles present at RT to the blocked state at such low temperature. To study this in detail we have recorded Zero field cooled (ZFC) and field cooled (FC) magnetizations of the samples and the observed values are compared in Fig. 4. We have recorded the ZFC and FC magnetizations of the samples at different temperatures from 300 K down to 10 K. The FC magnetization curve is recorded after cooling the sample in presence of an applied field of 500 Oe. From Fig. 4, we observe that FC and ZFC curves are bifurcated below RT. This bifurcation is observed due to the presence of the SPM relaxation in the nanoparticles. The blocking temperature for monodisperse magnetic nanoparticles is defined as the temperature below which the SPM relaxation is blocked. However, for magnetic nanoparticles with a size distribution, there is no particular temperature below which the phenomenon of blocking can be observed. In this type of sample, the blocking temperature will also be distributed according to the size distribution of the nanoparticles [35]. Thus, in case of a system with distributed particle size, the SPM relaxation blocking phenomenon is described by two temperatures (T_B and T_P). In this case, T_B is the temperature where ZFC and FC magnetizations are started to bifurcate due to larger group of particles and T_P is the temperature where ZFC magnetization shows maximum value in its thermal

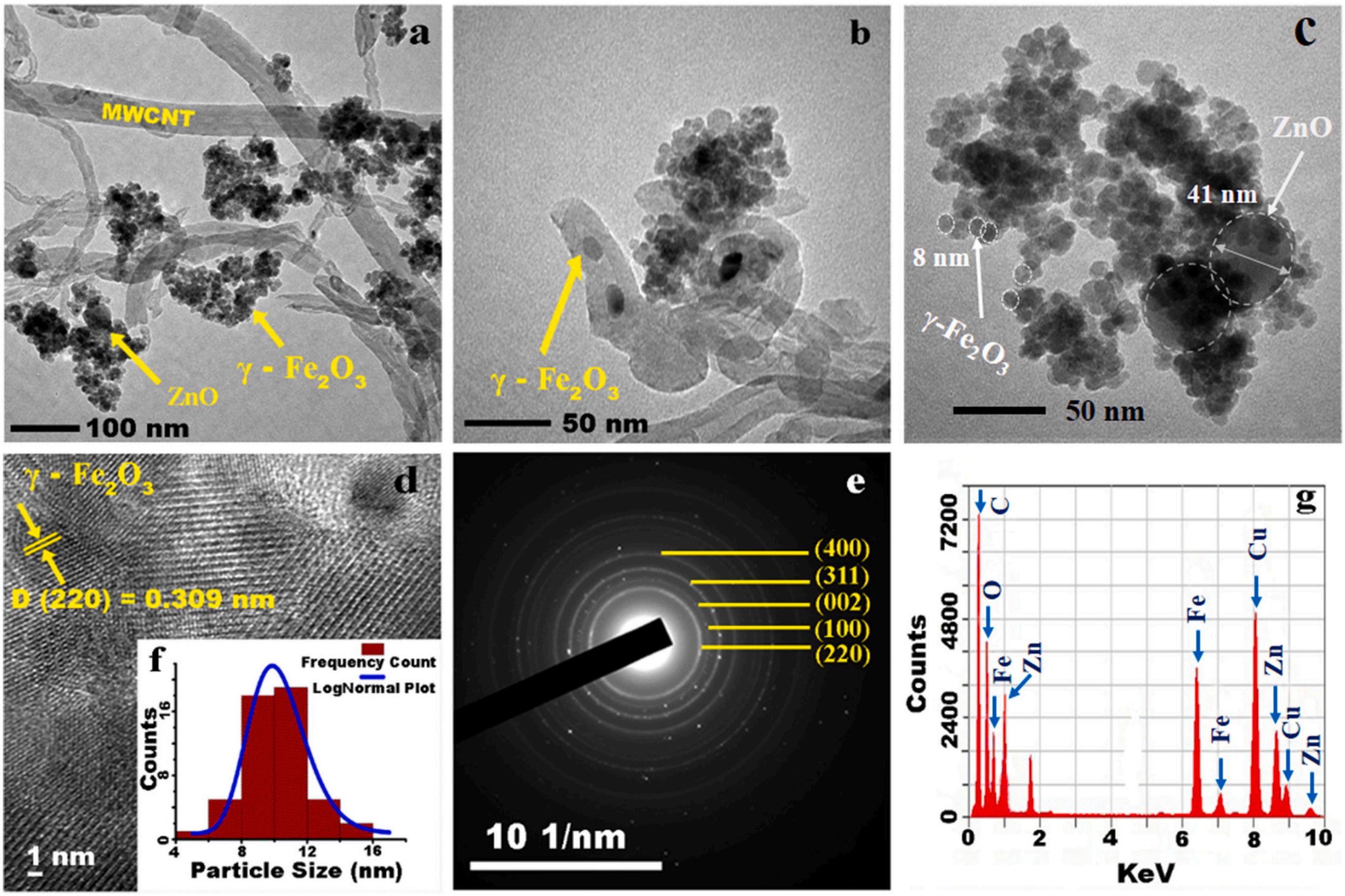

Fig. 2. (a - c) Micrographs (d) HRTEM Fringe pattern (e) SAED pattern (f) Particle size distribution of γ-Fe_2O_3 (g) EDAX of the FZ@MWCNT sample.

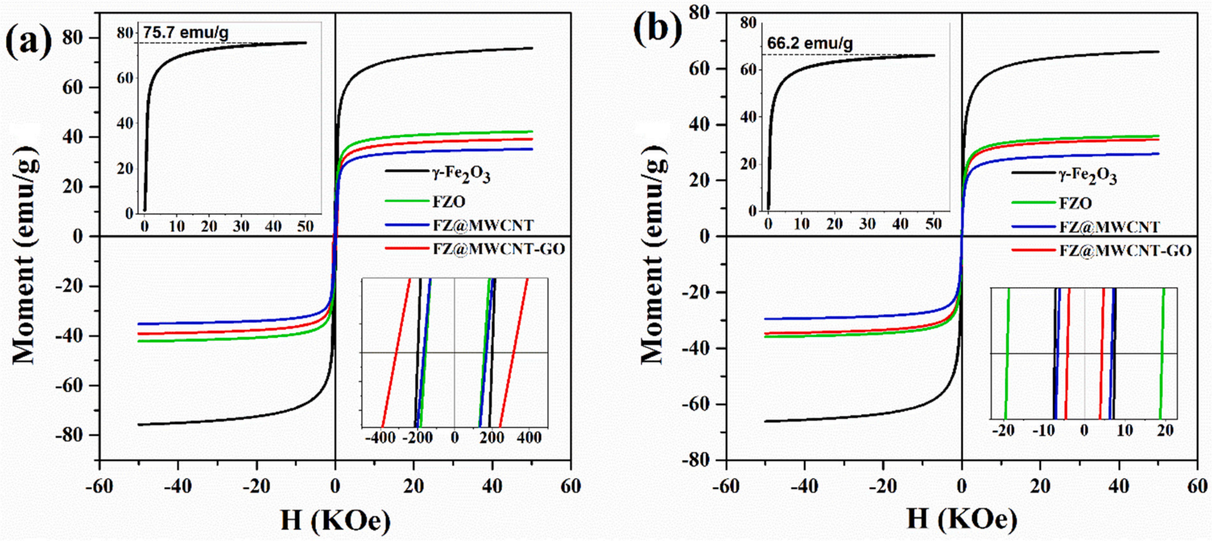

Fig. 3. (a) MH at 10 K (b) MH at 300 K of the γ-Fe_2O_3, FZO, FZ@MWCNT and FZ@MWCNT-GO sample.

variation. After T_P ZFC magnetization decreases due to smaller groups of particles in the system and T_P is lower than T_B. Here in the present case also, we get distinct values of T_B and T_P. The values of T_B are 250 K, 242 K, 240 K and 235 K and T_P values are 64 K, 62 K, 61 K, and 59 K as obtained from the graph for the γ-Fe_2O_3, FZO, FZ@MWCNT, and FZ@MWCNT-GO samples respectively. Thus from the above observation we see that the samples are in mixed phase of ordered magnetic particle with fraction of SPM nanoparticles. From the M-H loops of the samples, we observe that the value of M_S has decreased systematically in FZO, FZ@MWCNT as compared to γ-Fe_2O_3 due to the introduction of non-magnetic component like ZnO and MWCNT in the composite state. However, the value of M_S of FZ@MWCNT-GO is little bit higher as compared to FZ@MWCNT, although the fraction of non-magnetic components is same in both the samples. This fact can be explained

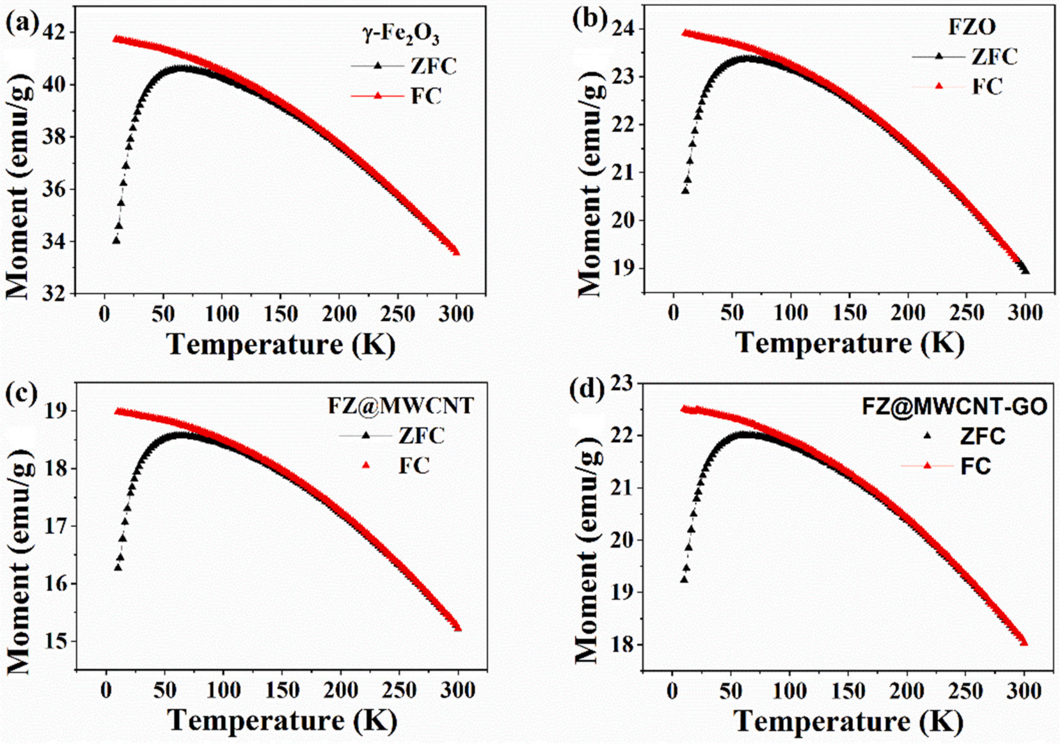

Fig. 4. MT measurement of the samples at 500 Oe (a) γ-Fe_2O_3 (b) FZO (c) FZ@MWCNT (d) FZ@MWCNT-GO.

due to the charge transfer effect or due to the existence of various defects on GO that can shows the ferromagnetism [36,37]. Nanoparticles of γ-Fe_2O_3 and ZnO decorated over the MWCNT matrix induce notable magnetization which harmonizes the dielectric property to the magnetic property and provides the impedance matching.

4. Electromagnetic shielding effectiveness

A detailed experimental observation as electromagnetic shielding effectiveness in the microwave range and the analysis of the recorded absorption open a new challenge in this subject. Even today, there are so many diverse reports that have not allowed us to draw a definitive conclusion and here, an effort has been made to enrich the platform. EM wave shielding is accomplished by the total effectiveness of shielding (SE_T) and expressed in dB. It is a dissipated quantitative measure of the EM pulse. Overall, the shielding effectiveness can be ascribed to three components such as reflection (SE_R), absorption (SE_A), and multiple reflections (SE_{MR}) and is expressed by the following relation

$$SE_T = SE_A + SE_R + SE_{MR} \tag{1}$$

The value of $SE_T > 10$ dB implies that the material is capable of attenuating the signal by 90%. Fig. 5 shows an optical photo of measurement suits and depicts a schematic representation of EM wave shielding that illustrates the different attenuation mechanism of EM wave by absorbent materials. The attenuation of the EM wave within the sample occurs through a variety of relaxation or resonance mechanisms, while other essential factors, such as conductive loss, impedance matching, eddy current loss etc., are further explained in details in supplement copy S1.

SE_T in X and K_U band of frequencies depends on three basic components: specifically reflection from the incident surface, absorption of incident energy and multiple reflections. Besides, multiple reflections can be overlooked when SE_T is more than 10 dB [38] and in that case, eq. (1) can be recorded as

$$SE_T = SE_A + SE_R \tag{2}$$

SE_T is obtained from different scattering parameter S_{11}, S_{12}, S_{22}, S_{21} which are directly measured by VNA and expressed as [39].

$$SE_T(dB) = 10\,log_{10}\left(\frac{1}{S_{12}^2}\right) = 10\,log_{10}\left(\frac{1}{S_{21}^2}\right) \tag{3}$$

Now, SE_A and SE_R are defined as

$$SE_A = 10\,log_{10}\left(\frac{1 - S_{11}^2}{S_{12}^2}\right) \tag{4a}$$

$$SE_R = 10\,log_{10}\left(\frac{1}{1 - S_{11}^2}\right) \tag{4b}$$

Frequency depended reflection (R), transmission (T) and absorption (A) coefficients of the samples are shown in Fig. 6. R, T and A represent the reflected, transmitted and absorbed power of the sample and are calculated from the S parameters [40]. From Fig. 6a and Fig. 6c it is clear that FZ@MWCNT shows the maximum shielding mechanism through reflection at 12.4 GHz and 16 GHz where at the same frequency it shows the minimum absorption power. Also, Fig. 6b depicts that all the samples have almost zero transmitted power except paraffin wax which shows the maximum transmitted power. FZ@MWCNT has the dominating nature of reflection power loss over the FZ@MWCNT-GO sample whereas FZ@MWCNT-GO shows higher absorption power over FZ@MWCNT. This is due to the addition of GO to the sample which increases the attenuation power of the sample. All the samples shows its higher absorption values at the frequencies ~10 GHz, 14 GHz and 18 GHz where its surface impedance matching is improved. This fact is the clear indication that at that frequency regions EM wave penetrates the sample and attenuated inside the sample. Fig. 7a shows the SE_T in the frequency band of 8.2 to 18 GHz, where we can detect considerable shielding effectiveness due to the addition of MWCNT. Maximum SE_T for the sample, FZ@MWCNT is −36.9 dB at 15.7 GHz holding sample thickness 3.5 mm, and further improvement is noticed for the addition of GO matrix where SE_T is −56.7 dB with same sample thickness. A comparison of current work with some publications is reported in Table 1.

The amplitude of the transmitted EM wave depends on the imped-

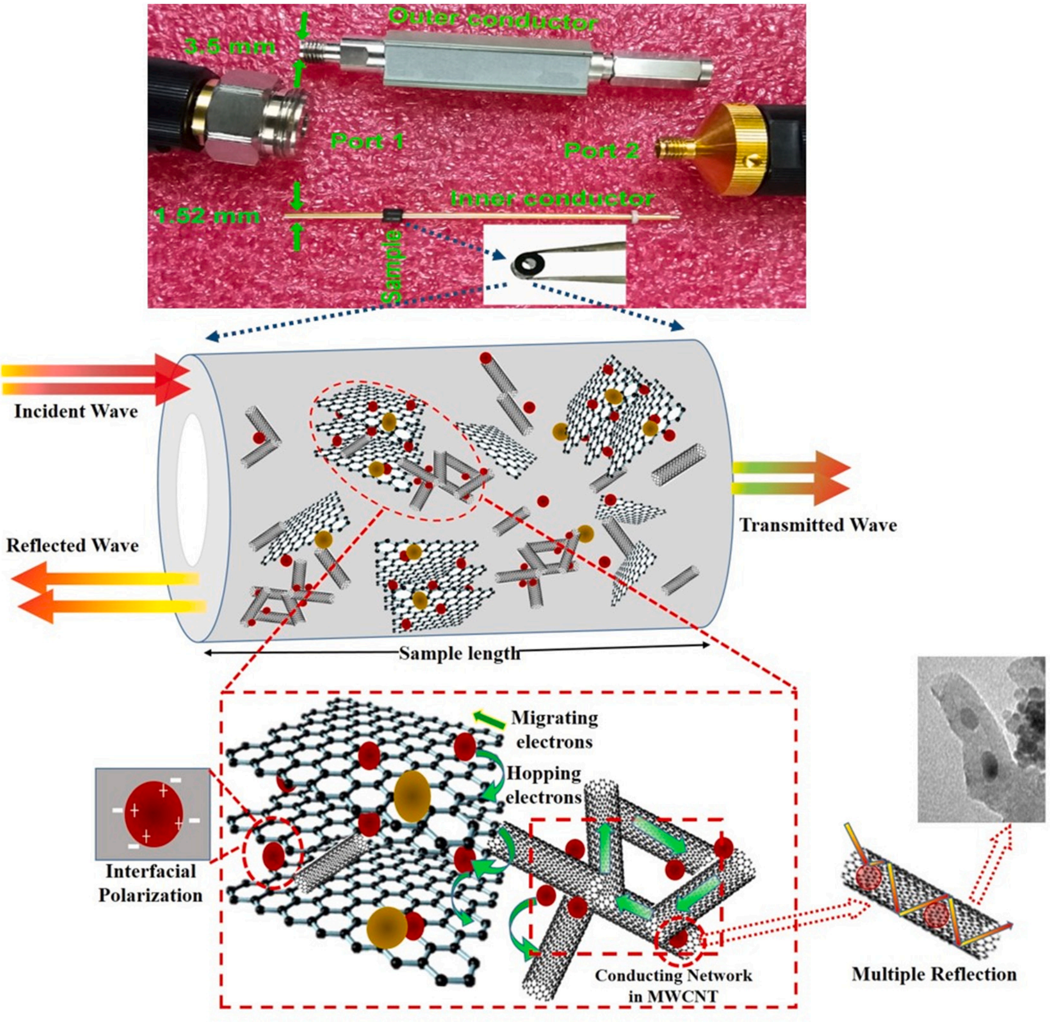

Fig. 5. Optical photo and Pictorial illustration of EM wave shielding effectiveness.

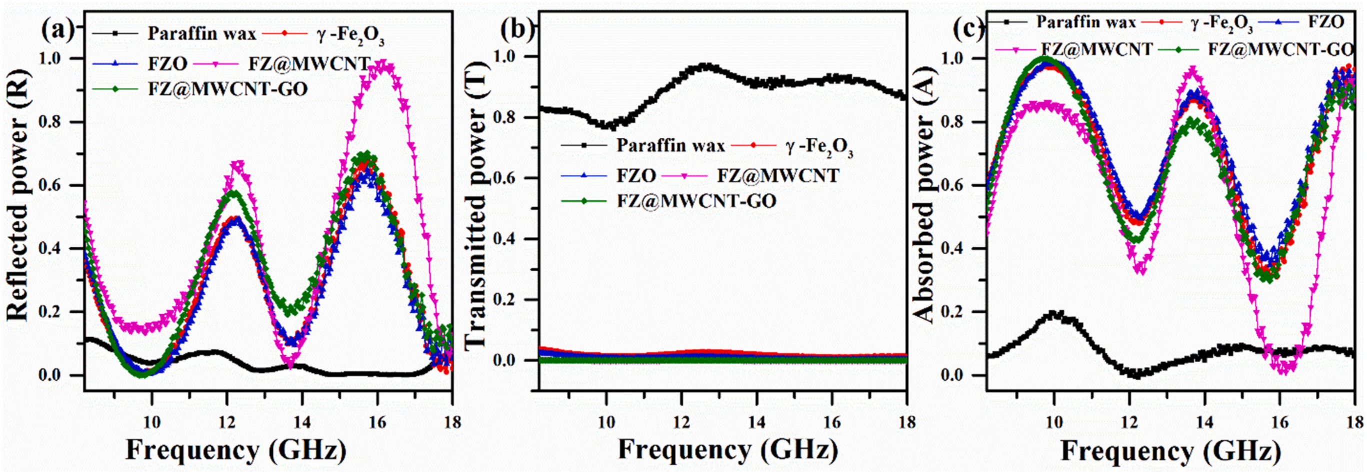

Fig. 6. Frequency dependent (a) Reflected power (b) Transmitted power and (c) Absorbed power of all the samples.

ance of the shielding material that decays exponentially due to absorption. Therefore, in the first part, reflection from the incident surface should be the primary concern, i.e., the impedance matching of the sample with the air and the value of this characteristic impedance should be expected to 1 for more efficient penetration of EM wave [38,49]. The characteristic impedance is estimated by the ratio of the real part of permittivity to permeability. If the real part of permittivity is extremely high from the real part of permeability, most of the EM wave will be reflected due to the low surface impedance. Under this circumstance, the magnitude of reflection can be estimated as [50].

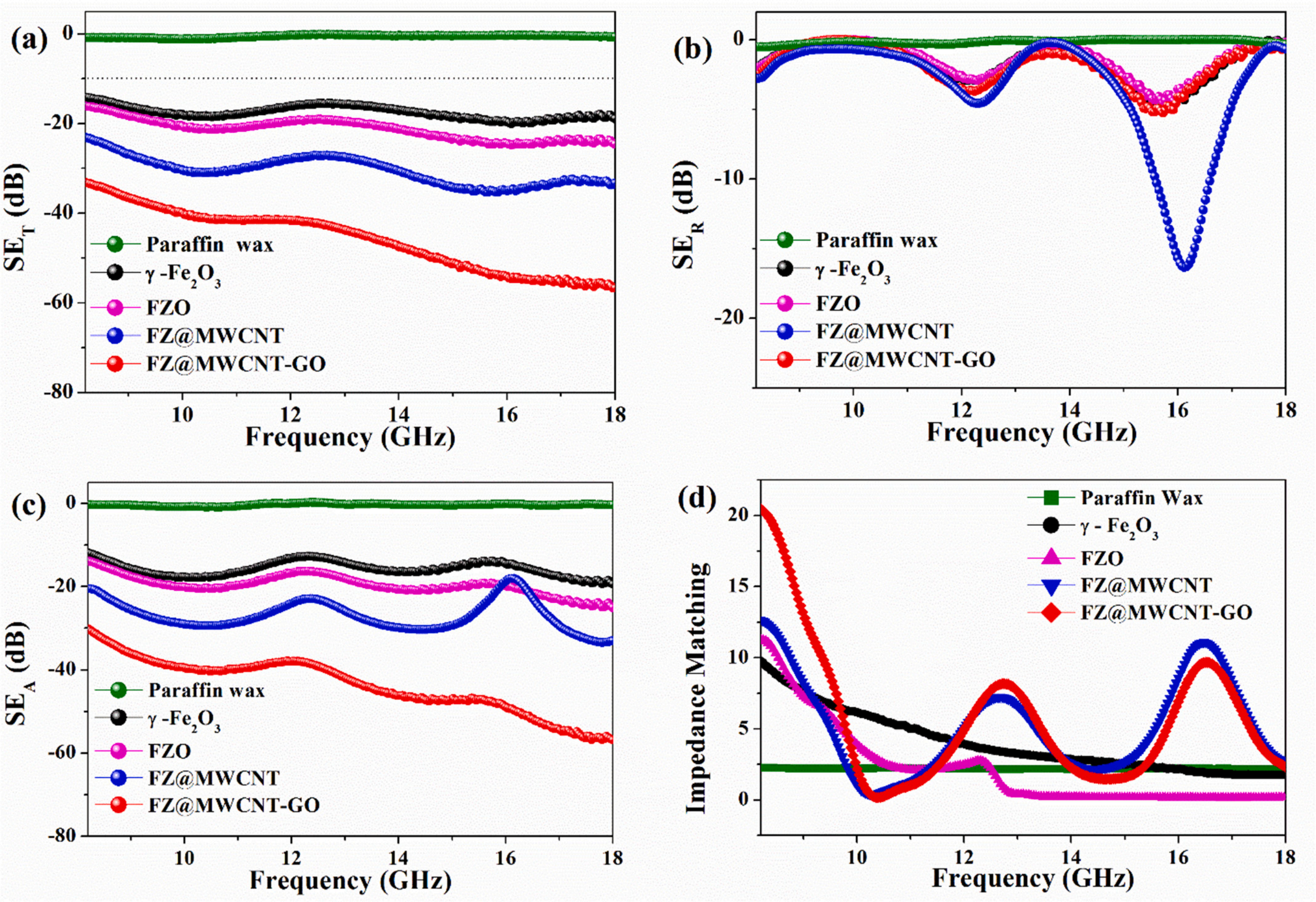

Fig. 7. (a) Total shielding effectiveness (b) Shielding effectiveness through reflection (c) Shielding effectiveness through absorption (d) Impedance matching factor.

Table 1
Comparison of present work with some previously published reports.

Sr. no.	Matrix	System	Frequency (GHz)	Sample thick-ness (mm)	Measurement method	SE_T (dB)	Ref.
1	PANI	Fe_3O_4	K_U – bBand	–	Waveguide	- 16.8	[41]
2	Polyetherimid	Graphene@Fe_3O_4 (10 wt%)	X- band	2.5	Scalar measurement	- 17.8	[42]
3	Polystyrene	Fe_3O_4@graphene (2.24 vol% graphene)	8–12	–	Scalar measurement	- 30	[43]
4	Polyaniline	Graphene – Fe_3O_4 (66.6%)	K_U – bBand	3.34	Waveguide	- 26	[44]
5	PVP – Paraffin wax	Fe_3O_4 - MWCNT	2–18	3	Coaxial	- 35.8	[45]
6	PS	MWCNT (2 wt%), graphene (1.5 wt%)	X- band	–	Industrial standard method	- 20.2	[46]
7	PC/SAN blend	MWCNT grafted Fe_3O_4	X and K_U -band	5	Coax	- 32.5	[47]
8	–	MWCNT/Fe_3O_4@ZnO	X- band	–	–	- 40.9	[17]
9	PC/SAN	rGO – Fe_3O_4(10 wt%) + MWCNT(3 wt %)	8–18	5	Coax	- 50.7	[48]
10	PC/PVDF	MWCNT - MnO_2 + rGO - Fe_3O_4	8–18	0.9	Waveguide	- 36	[38]
11	CNT	γ-Fe_2O_3	X band	2	Waveguide	- 32	[29]
12	Paraffin wax	FZ@MWCNT	8.2–18	3.5	Coaxial - airline	- 36.9	Present work
13	Paraffin wax	FZ@MWCNT-GO	8.2–18	3.5	Coaxial - airline	- 56.7	Present work

$$SE_R = -10\, log_{10}\left(\frac{\sigma_T}{16\varepsilon_0\omega\mu_r}\right) \tag{5}$$

Here σ_T and μ_r represent conductivity and relative permeability. From this relation, it is obvious that the reflection of the EM wave is proportional to the ratio of conductivity and permeability of the sample. Fig. 7b indicates the presence of a larger quantity of MWCNT in the FZ@MWCNT sample as SE_R value for this sample is higher than other samples. This is due to the highly conductive nature of MWCNT. For γ-Fe_2O_3 and FZO samples, EM wave is reflected from the incident surface because of impedance mismatch. Besides, from Fig. 7b and d, due to the addition of GO to the FZ@MWCNT sample, the conductivity, as well as the relative permeability, harmonized in a certain manner at which the EM wave penetrates more at specific frequencies where the impedance matches more to the air impedance, and the SE_A value increases (Fig. 7c). From Fig. 7d, we notice that the impedance matching for the sample FZ@MWCNT and FZ@MWCNT-GO has restricted to air impedance at 11 to 12 GHz and 15 to 16 GHz, respectively. So the EM wave penetrated more at the mentioned frequency ranges and this penetration power for paraffin wax is more or less constant for the full band of frequency ranges, and well-matched to the outer. Thus, the EM wave in this frequency range may be considered as transparent for the paraffin wax sample. Conductivity variation of the samples is shown in Fig. 8a where paraffin wax shows almost zero conductive nature. Due to the addition of FZO, conductivity increases whereas FZ@MWCNT-GO reveals high conductive nature due to percolation threshold polarization and capacitive coupling between the nanoparticles and GO. It is well understood that rather than very high electrical conductivity, a connecting network of conducting phase which can provide the free charge carrier is crucial for better EM attenuation. In the case of FZ@MWCNT-GO sample, the concentration of MWCNT is comparatively lower than that of the FZ@MWCNT sample so that a lower filler concentration facilitates the arrangement of the connecting network rather than a high conductivity. Fig. 8b depicts that the skin depth of the FZO sample is very low and decreases its value with the increase of frequency which attributed to the increased cross-linking and interfacial polarization. For paraffin wax sample calculated skin depth value is 1.98 mm at 8.2 GHz which is significantly higher than FZO. As sample thickness is more than the skin depth, multiple reflection has a deteriorative effect on SE_T value [48]. In this case, the multiple reflections of the EM wave inside the MWCNT surface (very high specific surface area) attenuate the energy of the wave mainly by absorption rather than by reflection.

In addition to the loss parameter, as mentioned above, the attenuation constant (α) is also a crucial factor that enhances the absorption ability of the material [51,52]. The large value of the attenuation factor signifies the penetration power of EM wave to the absorber and after that, the attenuation or absorption of EM waves in this absorber. The curves in Fig. 9c confirms that the attenuation factor of FZ@MWCNT is lower than that of FZ@MWCNT-GO due to the increase of permittivity and permeability parameter. This attenuation amount presents its high peaks at the frequency region where maximum absorption occurs. For the sample γ-Fe_2O_3 and FZO, the attenuation factor value is quite less than the value for FZ@MWCNT and FZ@MWCNT-GO. Therefore, due to the incorporation of heterogeneous nanoparticles into the matrix, both the attenuation factor and loss parameter increase simultaneously. In the case of paraffin wax, this reaches approximately zero value, which is why it has no shielding effectiveness value.

As the nature of EM wave is oscillatory in the context of its polarity, this type of motion initially induces misalignment between the electric field of incident EM wave with the charge distribution of nanoparticles. Where this type of displacement occurs inside the nanomaterials (via the force of applied electric field) a potential is generated within the material due to displacement of its original state manifesting as a subsequent generation of heat. After depositing nanocomposites within the polymer, abundant polarizations (defect polarization, heterogeneous interfacial polarization and residual functional groups) forming a mass of dipoles are introduced. At high-frequency, these mass dipoles establishes the relaxation mechanisms and transform the EM energy into heat energy [53]. Similarly, for the case of an external magnetic field, the intrinsic and extrinsic magnetic field of nanomaterials align with the incident magnetic field part of EM wave. This creates a potential within the nanomaterials, as in the case of charged particles with permittivity and alleged thermal energy dissipation i.e. potential degradation [54]. From theoretical explanation when a high-frequency EM wave encounters a volume through the surface, then it partially reinforces the field energy stored inside this volume and the rest is dissipated as heat energy. The energy distribution occurs when the damping force acts on the polarized atoms or molecules and conductivity of the material. The absorption of EM wave is due to the energy loss and the subsequent dissipation as heat. However, to shield the EM wave, both the electric and magnetic dipoles are essential as the EM wave is the synchronized generation of electric and magnetic dipole vectors. Tactically, the energy conversion of EM wave is transforming of different dipolar relaxation or resonances and switching these electrically and magnetically generated potential to heat energy [55]. The relative permittivity ($\varepsilon = \varepsilon' - \varepsilon''$) and permeability ($\mu = \mu' - \mu''$) of the materials contains the storage part (ε' and μ') via polarization mechanism and alignment of magnetic dipoles along the direction of magnetic field and energy dissipation part (ε'' and μ'') resulting from conduction, relaxation and resonance mechanism [56]. From Fig. 9a and b it can be observed that ε' and ε'' values for the samples FZ@MWCNT and FZ@MWCNT-GO are more than those for the samples γ-Fe_2O_3 and FZO. The real part of permittivity for all the samples represents a declining trend with the increase of frequency because of frequency dispersion behavior whereas there is no such declining trend in case of the imaginary part of permittivity, an obvious sign of dielectric relaxation of the samples [57,58]. However, in the case of FZ@MWCNT and FZ@MWCNT-GO, fluctuations are observed in both $\varepsilon'$and ε'' due to the incoherence of Debye polarization with that of the incident EM wave [59]. Moreover, the permittivity curve intimates the significant increase in ε' with the addition of MWCNT and GO. From the above characteristics of $\varepsilon'$and ε'', there is a precise estimation on the increment of the ratio of ε'' to ε', which is understood as the dielectric tan losses. The dielectric losses mainly originate from conductivity loss and polarization loss where polarization loss could be additionally classified as ionic, electronic, interfacial and dipole orientation polarization [60]. However, here only the interfacial polarization (space charge polarization) is significant because the others such as ionic and electric polarization are caused in the excessive high-frequency region only. The defect dipoles and interfacial dipoles are influenced by the charge imbalance in the lattice while interfacial dipoles occurs between the lattice interfaces. As the relaxation time for grain boundary regions is larger than that for bulk, the grain boundary response relaxes at lower frequencies than the bulk [61]. Although polarization plays a fundamental role in the imaginary part of permittivity, the free electrons, i.e. the electrical conductivity are more ruling on it. According to free-

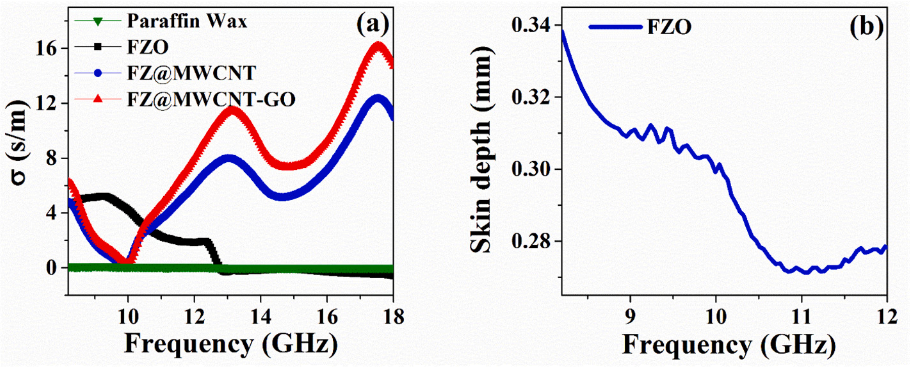

Fig. 8. (a) Conductivity and (b) Skin depth variation as a function of frequency.

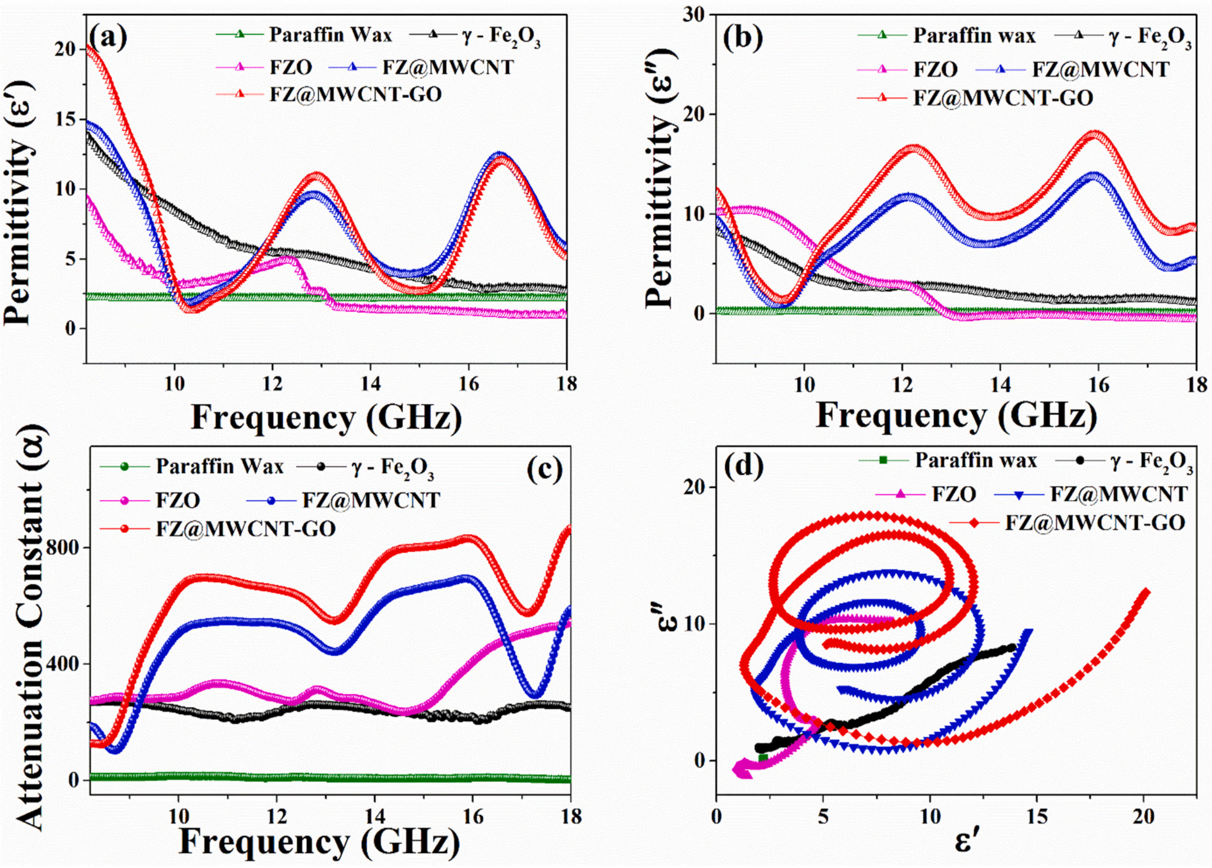

Fig. 9. (a) Real Part of Permittivity (b) Imaginary Part of Permittivity (c) Attenuation Constant (d) Cole-Cole plot.

electron theory [62]

$$\varepsilon'' \approx \frac{\sigma(T)}{2\pi\varepsilon_0 f} \tag{6}$$

Where σ(T) is the temperature-dependent electrical conductivity, which presents the dominating role in ε'', f the frequency and ε_0 the vacuum permittivity. Electrical conductivity, i.e. both migrating conductance in the GO plane and hopping conductance among disordered GO layers, increases with increasing temperature and frequency [62]. Moreover, this increment in conductivity further enhances the imaginary part of permittivity.

The Cole-Cole plots (Fig. 9d) of ε'vs. ε'' are carried out to explain the dielectric relaxation nature in the composite material. According to the Debye dielectric relaxation approach, the relation between ε' and ε'' can be formulated as [63]

$$\left(\varepsilon' - \varepsilon'_\infty\right)^2 + \left(\varepsilon''\right)^2 = \left(\varepsilon'_0 - \varepsilon'_\infty\right)^2 \tag{7}$$

Where ε_0' and ε_∞' signifies the static dielectric constant and the dielectric constant at the highest frequency. Thus the individual Debye relaxation process is assigned by a semicircle identified as Cole-Cole semicircle. From the plot, we can remark that only one distinguishable semicircle is observed for γ-Fe_2O_3 sample, implying the sole relaxation process. However, more than one semicircle is projected for the samples FZ@MWCNT and FZ@MWCNT-GO where individual semicircle resembles Debye dipole relaxation. The enhanced polarization relaxation may originate from the defects of MWCNTs, which can serve as a polarization center under the alternating EM field. Furthermore, the abundant oxygenic functional group on the surface of MWCNT such as C = O and C - O can offer electronic dipole polarization [64,65]. The distorted portion of the semicircle, including the tails of the plots, reveals the other loss mechanism, such as leakage conductivity loss [66]. In the composite system, the electrons from the polymer may defeat the barrier and assembled at the interface of the heterojunction of the nanocomposite and build an interfacial polarization of space charge. Therefore after incorporation of γ-Fe_2O_3 and ZnO nanoparticles along with the conducting matrix, the value of SE_T increases significantly by several orders due to interfacial polarization and relaxation mechanism. The interfacial dielectric polarization of MWCNT and GO with nanoparticles results in the absorption of electric vector components whereas magnetic loss due to magnetic materials led to the absorption of the magnetic vector component of the incident EM wave.

Magnetic permeability of all samples is shown in Fig. 10 where μ″ of FZ@MWCNT-GO delivers the resonance peaks at 9.5 GHz, 10.9 GHz, 13.3 GHz and 17.2 GHz. Magnetic materials with high saturation magnetization also provide high initial magnetic permeability and high initial magnetic permeability can be predicted to have a high magnetic loss. Magnetic loss mainly results from magnetic hysteresis, natural resonance, exchange resonance, domain-wall displacement, and eddy current effect [67,68]. Since the incident EM waves have a shallow magnetic field and a very high frequency, the loss of hysteresis and the displacement effect of the domain wall can be excluded. The loss of hysteresis plays a role in irreversible magnetization and can be neglected for the weak field. Domain wall resonance occurs only in the 1–100 MHz range and for multi-domain materials. Finally, natural resonance, exchange resonance and eddy current effects are recognized as the most responsible factors for high-frequency magnetic losses whereas natural resonance normally occurs to a lower frequency than the exchange resonance [69].

Furthermore, the eddy current loss coefficient can be expressed as

$$\frac{\mu''}{f(\mu')^2} \approx \frac{2\pi\mu_0 d^2}{3\rho} \tag{8}$$

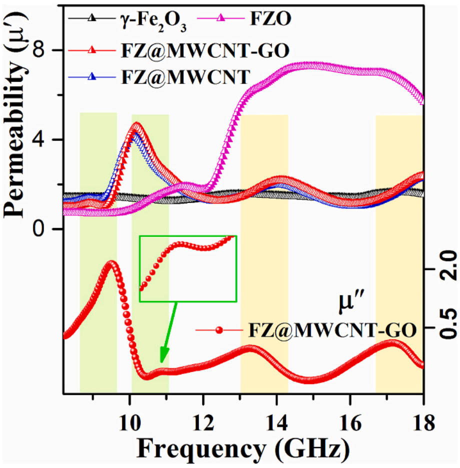

Fig. 10. Magnetic permeability of all samples and $\mu''$of FZ@MWCNT-GO.

Where *f*, d, and ρ correspond to the frequency, the diameter and the electric resistivity of the particle, respectively. We can see from Fig. 11a that the eddy current loss for the sample, γ-Fe_2O_3 is almost constant, i.e. independent of frequency which indicates that the magnetic permeability losses are obtained by eddy current loss [49,70] whereas dissipated energy is correlated with the dielectric tangent loss (tan $\delta_\varepsilon = \varepsilon''/\varepsilon'$) and the magnetic tangent loss (tan $\delta_\mu = \mu''/\mu'$). With this consideration, we inspected from Fig. 11b that the total loss increases due to the addition of MWCNT and further improvements are indicated for the acquisition of GO in the bare composite of FZ@MWCNT sample. In the case of paraffin wax total tan loss value is almost zero, which is why it is unable to absorb the EM wave. For the composite samples FZ@MWCNT and FZ@MWCNT-GO, we attained two peaks values of the tan loss at the region where these samples give a maximum shielding loss. We ensure that the charge transport mechanism of electron hopping and/or tunneling initiate conductivity losses and interfacial polarization of γ-Fe_2O_3 and ZnO nanocomposite in MWCNT and GO matrix ensures a positive contribution to the dielectric loss as well as energy conversion. Therefore, when the incoming EM wave reaches the sample, it passes the sample across various microscopic boundaries due to the inclusion of different nanocomposites, such as γ-Fe_2O_3 and ZnO, which constitute the heterostructure. At the interface of two materials i.e., on the heterogeneous edges, the accumulated virtual charge significantly absorbs the wave energy through Joule heating and may change the local fields which in turn can alter the EM wave as it varies quadratically with field intensity [40]. The thermal conductivity of the sample further improves due to the enhancement of heterogeneous nanoparticles, and thus, the generated heat can easily spread-out. In addition, the shape and size of these nanoparticles present an imperative role of dispersion in the matrix. The absorption property of microwave increases with the reduction in particle sizes, i.e. on the excellent distribution of nanoparticles. Nanomaterials' size and shape or composition may change the dielectric/magnetic properties to ensure a good match for microwave absorption between them. When particle size decreases and crystallinity increases (compare with the amorphous nanoparticles), the active surface of the nanoparticles increases, and therefore the interaction with the nanoparticles developed [71] which further increases the eddy current loss, resonance effect and subsequently increase the absorption loss [72].

5. Conclusions

We have succeeded in synthesizing new shielding materials with unusual efficiency and cost-effectiveness using a simple and unconventional method where the absorption efficiency of these materials is remarkably high. They are based on a suitable combination of dielectric and magnetic materials in the nanocomposite that consolidates into the MWCNT and GO matrices supporting the material for corrosion resistance. To achieve this efficiency, we have also adopted several novel approaches that are duly discussed in various sections. In addition, here we have invoked an efficient approach in the measurement procedure based on the coaxial linear method and this technique is more effective for practical purposes than the reflection loss measuring technique used by several previous researchers including our investigations. The microstructure analysis gives the cluster like formation of nanoparticles in the nanocomposite due to the π interaction bond by magnetophoresis. The results of magnetic measurements for FZ@MWCNT and FZ@MWCNT-GO explain well the relatively low saturation magnetization due to the presence of non-magnetic graphite coating with a strong magnetic component of γ-Fe_2O_3 nanoparticles. The incorporation of nanoparticles in these matrices amplifies the complex permittivity as well as permeability due to the presence of high dielectric carbon and magnetic nanoparticles in the desired frequency range. The influence of the MWCNT and GO matrices in the nanocomposite system is also studied in detail for the increased activity. The dielectric losses attributed to the Debye relaxation and also the conductivity losses are strongly responsible for the improved absorption of EM waves. The presence of maghemite nanoparticles introduces magnetic losses by resonance and eddy current effect, while the presence of other nanoparticles in the composite promulgates dielectric losses influenced by polarization and conductivity losses. The coincidence and coherence effect of these losses in the present nanocomposite may open the opportunity of making a

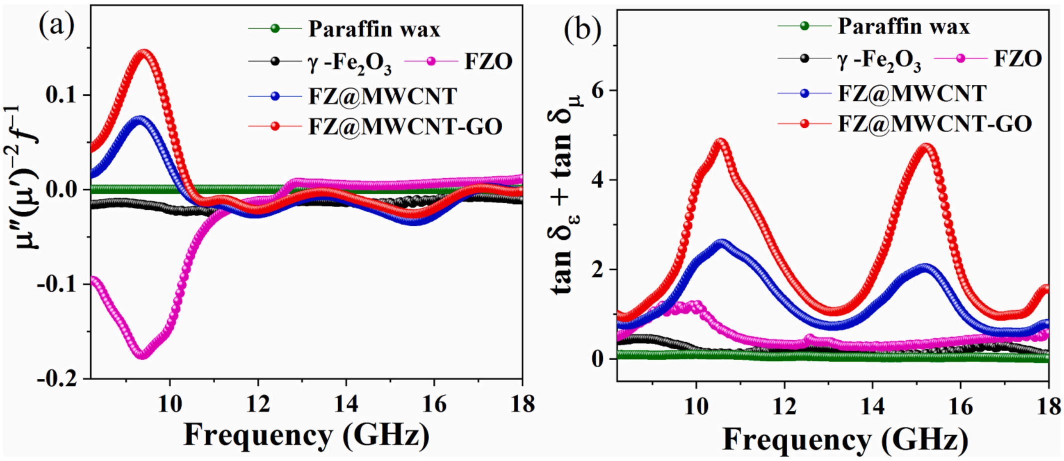

Fig. 11. (a) Eddy current loss co-efficient (b) Total tan loss.

good microwave absorbing material for better performance. A synthesis of these mechanisms is described schematically in this work.

Data availability statement

The Data that support the findings of this study are available from the corresponding author upon reasonable request.

Declaration of Competing Interest

The authors declare that they have no known competing financial interests or personal relationships that could have appeared to influence the work reported in this paper.

Acknowledgements

The authors wish to acknowledge the DST-SERB, GOVT OF INDIA (Order No: EMR/2017/000832, DATED: 19.03.2018) for the financial assistance of the present work. The authors also wish to acknowledge the financial support provided by UGC, Govt. of India, through the CAS program (No. F.530/20/CAS-II/2018 (SAP—I), DATED: 25.07.2018), FIST, DST Govt. of India (Ref: SR/FST/PS-II/2018/52, TPN No- 19862,) and PURSE-11, DST, Govt. of India (No. SR/PURSE Phase-2/34, DATED: 27.02.2017).

Appendix A. Supplementary data

Supplementary data to this article can be found online at https://doi.org/10.1016/j.matchar.2021.110884.

References

[1] X.X. Wang, W.Q. Cao, M.S. Cao, J. Yuan, Assembling nano–microarchitecture for electromagnetic absorbers and smart devices, Adv. Mater. 32 (2020) 2002112.

[2] H. Zhang, C. Shi, Z. Jia, X. Liu, B. Xu, D. Zhang, G. Wu, FeNi nanoparticles embedded reduced graphene/nitrogen-doped carbon composites towards the ultra-wideband electromagnetic wave absorption, J. Colloid Interface Sci. 584 (2021) 382–394.

[3] H. Zhang, Z. Jia, A. Feng, Z. Zhou, L. Chen, C. Zhang, X. Liu, G. Wu, In situ deposition of pitaya-like Fe_3O_4 magnetic microspheres on reduced graphene oxide nanosheets for electromagnetic wave absorber, Compos. Part B 199 (2020) 108261.

[4] P. Sambyal, A. Iqbal, J. Hong, H. Kim, M.K. Kim, S.M. Hong, M. Han, Y. Gogotsi, C. M. Koo, Ultralight and mechanically robust Ti3C2Tx hybrid aerogel reinforced by carbon nanotubes for electromagnetic interference shielding, ACS Appl. Mater. Interf. 11 (2019) 38046–38054.

[5] F. Zhang, W. Cui, B. Wang, B. Xu, X. Liu, X. Liu, Z. Jia, G. Wu, Morphology-control synthesis of polyaniline decorative porous carbon with remarkable electromagnetic wave absorption capabilities, Compos. Part B 204 (2021) 108491.

[6] M.S. Cao, X.X. Wang, M. Zhang, J.C. Shu, W.Q. Cao, H.-J. Yang, X.Y. Fang, J. Yuan, Electromagnetic response and energy conversion for functions and devices in low-dimensional materials, Adv. Funct. Mater. 29 (2019) 1807398.

[7] B. Zhao, X. Guo, W. Zhao, J. Deng, G. Shao, B. Fan, Z. Bai, R. Zhang, Yolk–Shell Ni@SnO2 composites with a designable interspace to improve the electromagnetic wave absorption properties, ACS Appl. Mater. Interf. 8 (2016) 28917–28925.

[8] Y. Wang, X.M. Wu, W.Z. Zhang, C.Y. Luo, J.H. Li, Y.J. Wang, Fabrication of flower-like Ni0.5Co0.5(OH)(2)@PANI and its enhanced microwave absorption performances, Mater. Res. Bull. 98 (2018) 59–63.

[9] H. Lv, Z. Yang, P.L. Wang, G. Ji, J. Song, L. Zheng, H. Zeng, Z.J. Xu, A voltage-boosting strategy enabling a low-frequency, flexible electromagnetic wave absorption device, Adv. Mater. 30 (2018) 1706343.

[10] A.K. Singh, A. Kumar, K.K. Haldar, V. Gupta, K. Singh, Lightweight reduced graphene oxide-Fe3O4 nanoparticle composite in the quest for an excellent electromagnetic interference shielding material, Nanotechnology 29 (2018) 245203.

[11] H. Zhang, M. Hong, P. Chen, A. Xie, Y. Shen, 3D and ternary rGO/MCNTs/Fe3O4 composite hydrogels: synthesis, characterization and their electromagnetic wave absorption properties, J. Alloy Compd 665 (2016) 381–387.

[12] C. Han, M. Zhang, W.-Q. Cao, M.-S. Cao, Electrospinning and in-situ hierarchical thermal treatment to tailor C–NiCo2O4 nanofibers for tunable microwave absorption, Carbon 171 (2021) 953–962.

[13] B. Zhao, G. Shao, B.B. Fan, W.Y. Zhao, R. Zhang, Investigation of the electromagnetic absorption properties of Ni@TiO2 and Ni@SiO2 composite microspheres with core-shell structure, Phys. Chem. Chem. Phys. 17 (2015) 2531–2539.

[14] C. Wang, V. Murugadoss, J. Kong, Z. He, X. Mai, Q. Shao, Y. Chen, L. Guo, C. Liu, S. Angaiah, Z. Guo, Overview of carbon nanostructures and nanocomposites for electromagnetic wave shielding, Carbon 140 (2018) 696–733.

[15] L. Zhu, X. Zeng, M. Chen, R. Yu, Controllable permittivity in 3D Fe3O4/CNTs network for remarkable microwave absorption performances, RSC Adv. 7 (2017) 26801–26808.

[16] X. Jian, B. Wu, Y. Wei, S.X. Dou, X. Wang, W. He, N. Mahmood, Facile synthesis of Fe3O4/GCs composites and their enhanced microwave absorption properties, ACS Appl. Mater. Interf. 8 (2016) 6101–6109.

[17] Z. Wang, L. Wu, J. Zhou, Z. Jiang, B. Shen, Chemoselectivity-induced multiple interfaces in MWCNT/Fe3O4@ZnO heterotrimers for whole X-band microwave absorption, Nanoscale 6 (2014) 12298–12302.

[18] A.P. Singh, M. Mishra, D.P. Hashim, T.N. Narayanan, M.G. Hahm, P. Kumar, J. Dwfuedi, G. Kedawat, A. Gupta, B.P. Singh, A. Chandra, R. Vajtai, S.K. Dhawan, P.M. Ajayan, B.K. Gupta, Probing the engineered sandwich network of vertically aligned carbon nanotube-reduced graphene oxide composites for high performance electromagnetic interference shielding applications, Carbon 85 (2015) 79–88.

[19] H. Hekmatara, M. Seifi, K. Forooraghi, Microwave absorption property of aligned MWCNT/Fe3O4, J. Magn. Magn. Mater. 346 (2013) 186–191.

[20] C. Tsonos, N. Soin, G. Tomara, B. Yang, G.C. Psarras, A. Kanapitsas, E. Siores, Electromagnetic wave absorption properties of ternary poly(vinylidene fluoride)/magnetite nanocomposites with carbon nanotubes and graphene, RSC Adv. 6 (2016) 1919–1924.

[21] J. Guo, H.X. Song, H. Liu, C.J. Luo, Y.R. Ren, T. Ding, M.A. Khan, D.P. Young, X. Y. Liu, X. Zhang, J. Kong, Z.H. Guo, Polypyrrole-interface-functionalized nano-magnetite epoxy nanocomposites as electromagnetic wave absorbers with enhanced flame retardancy, J. Mater. Chem. C 5 (2017) 5334–5344.

[22] Y. Wang, Y. Song, Q. Qi, W. Wang, D. Yu, Robustly magnetic and conductive textile with high electromagnetic shielding performance prepared by synchronous thiol−Ene click chemistry, Ind. Eng. Chem. Res. 58 (2019) 23154–23165.

[23] K. Wang, G. Wan, G. Wang, Z. He, S. Shi, L. Wu, G. Wang, The construction of carbon-coated Fe3O4 yolk-shell nanocomposites based on volume shrinkage from the release of oxygen anions for wide-band electromagnetic wave absorption, J. Colloid Interface Sci. 511 (2018) 307–317.

[24] P. Wang, J. Zhang, G. Wang, B. Duan, D. He, T. Wang, F. Li, Synthesis and characterization of MoS2/Fe@Fe3O4 nanocomposites exhibiting enhanced microwave absorption performance at normal and oblique incidences, J. Mater. Sci. Technol. 35 (2019) 1931–1939.

[25] G. Wang, Z. Gao, S. Tang, C. Chen, F. Duan, S. Zhao, S. Lin, Y. Feng, L. Zhou, Y. Qin, Microwave absorption properties of carbon Nanocoils coated with highly controlled magnetic materials by atomic layer deposition, ACS Nano 6 (2012) 11009–11017.

[26] B. Wen, M. Cao, M. Lu, W. Cao, H. Shi, J. Liu, X. Wang, H. Jin, X. Fang, W. Wang, J. Yuan, Reduced graphene oxides: light-weight and high-efficiency electromagnetic interference shielding at elevated temperatures, Adv. Mater 26 (2014) 3484–3489.

[27] O. Balci, E.O. Polat, N. Kakenov, C. Kocabas, Graphene-enabled electrically switchable radar-absorbing surfaces, Nat. Commun. 6 (2015) 6628.

[28] A. Khaleel, M. Parvin, M. AlTabaji, A. Al-Zamly, Ti(IV)-doped gamma-Fe2O3 nanoparticles possessing unique textural and chemical properties: enhanced suppression of phase transformation and promising catalytic activity, J. Solid State Chem. 259 (2018) 91–97.

[29] S. Sutradhar, S. Das, A. Roychowdhury, D. Das, P.K. Chakrabarti, Magnetic property, Mössbauer spectroscopy and microwave reflection loss of maghemite nanoparticles (γ-Fe2O3) encapsulated in carbon nanotubes, Mater. Sci. Eng. B 196 (2015) 44–52.

[30] J.A. Ramos Guivar, A. Bustamante, J. Flores, M. Mejía Santillan, A.M. Osorio, A. I. Martínez, L. De Los Santos Valladares, C.H.W. Barnes, Mössbauer study of intermediate superparamagnetic relaxation of maghemite (γ-Fe 2 O 3) nanoparticles, Hyperfine Interact 224 (2013) 89–97.

[31] S. Chikazumi, Physics of ferromagnetism, Oxf. Sci. Publ. 201 (1997).

[32] A.R.A. Fattah, T. Majdi, A.M. Abdalla, S. Ghosh, I.K. Puri, Nickel nanoparticles entangled in carbon nanotubes: novel ink for nanotube printing, ACS Appl. Mater. Interf. 8 (2016) 1589–1593.

[33] É.d.T.d. LACHEISSERIE, D. Gignoux, M. Schlenker, Magnetism: Materials and Applications 395, 2005.

[34] A. Mallick, A.S. Mahapatra, A. Mitra, J.M. Greneche, R.S. Ningthoujam, P. K. Chakrabarti, Magnetic properties and bio-medical applications in hyperthermia of lithium zinc ferrite nanoparticles integrated with reduced graphene oxide, J. Appl. Phys 123 (2018).

[35] S. Modak, S. Karan, S.K. Roy, P.K. Chakrabarti, Static and dynamic magnetic behavior of nanocrystalline and nanocomposites of (Mn0.6Zn0.4Fe2O4)(1−z)(SiO2)z (z=0.0,0.10,0.15,0.25), J. Appl. Phys. 108 (2010) 093912.

[36] Y. Wang, Y. Huang, Y. Song, X. Zhang, Y. Ma, J. Liang, Y. Chen, Room-temperature ferromagnetism of graphene, Nano Lett. 9 (2009) 220–224.

[37] C. Majumder, S. Bhattacharya, S.K. Saha, Anomalous large negative magnetoresistance in transition-metal decorated graphene: evidence for electron-hole puddles, Phys. Rev. B 99 (2019), 045408.

[38] S. Biswas, I. Arief, S.S. Panja, S. Bose, Absorption-dominated electromagnetic wave suppressor derived from ferrite-doped cross-linked graphene framework and conducting carbon, ACS Appl. Mater. Interf. 9 (2017) 3030–3039.

[39] R. Bera, S. Suin, S. Maiti, N.K. Shrivastava, B.B. Khatua, Carbon nanohorn and graphene nanoplate based polystyrene nanocomposites for superior electromagnetic interference shielding applications, J. Appl. Polym. Sci. 132 (2015).

[40] F. Ren, D. Song, Z. Li, L. Jia, Y. Zhao, D. Yan, P. Ren, Synergistic effect of graphene nanosheets and carbonyl iron–nickel alloy hybrid filler on electromagnetic interference shielding and thermal conductivity of cyanate ester composites, J. Mater. Chem. C 6 (2018) 1476–1486.

[41] P. Saini, V. Choudhary, N. Vijayan, R.K. Kotnala, Improved electromagnetic interference shielding response of poly(aniline)-coated fabrics containing dielectric and magnetic nanoparticles, J. Phys. Chem. C 116 (2012) 13403–13412.

[42] B. Shen, W. Zhai, M. Tao, J. Ling, W. Zheng, Lightweight, multifunctional polyetherimide/graphene@Fe3O4 composite foams for shielding of electromagnetic pollution, ACS Appl. Mater. Interf. 5 (2013) 11383–11391.

[43] Y. Chen, Y. Wang, H.-B. Zhang, X. Li, C.-X. Gui, Z.-Z. Yu, Enhanced electromagnetic interference shielding efficiency of polystyrene/graphene composites with magnetic Fe3O4 nanoparticles, Carbon 82 (2015) 67–76.

[44] K. Singh, A. Ohlan, V.H. Pham, S. Varshney, J. Jang, S.H. Hur, W.M. Choi, M. Kumar, S.K. Dhawan, B.S. Kong, J.S. Chung, Nanostructured graphene/Fe(3)O(4) incorporated polyaniline as a high performance shield against electromagnetic pollution, Nanoscale 5 (2013) 2411–2420.

[45] C. Zhao, A. Zhang, Y. Zheng, J. Luan, Electromagnetic and microwave-absorbing properties of magnetite decorated multiwalled carbon nanotubes prepared with poly(N-vinyl-2-pyrrolidone), Mater. Res. Bull. 47 (2012) 217–221.

[46] S. Maiti, N.K. Shrivastava, S. Suin, B.B. Khatua, Polystyrene/MWCNT/graphite nanoplate nanocomposites: efficient electromagnetic interference shielding material through graphite nanoplate-MWCNT-graphite nanoplate networking, ACS Appl. Mater. Interf. 5 (2013) 4712–4724.

[47] S.P. Pawar, D.A. Marathe, K. Pattabhi, S. Bose, Electromagnetic interference shielding through MWNT grafted Fe3O4 nanoparticles in PC/SAN blends, J. Mater. Chem. A 3 (2015) 656–669.

[48] S.P. Pawar, M. Gandi, S. Bose, High performance electromagnetic wave absorbers derived from PC/SAN blends containing multiwall carbon nanotubes and Fe3O4 decorated onto graphene oxide sheets, RSC Adv. 6 (2016) 37633–37645.

[49] S. Kumar, G. Datt, A.S. Kumar, A.C. Abhyankar, Enhanced absorption of microwave radiations through flexible polyvinyl alcohol-carbon black/barium hexaferrite composite films, J. Appl. Phys. 120 (2016).

[50] P. Saini, V. Choudhary, B.P. Singh, R.B. Mathur, S.K. Dhawan, Enhanced microwave absorption behavior of polyaniline-CNT/polystyrene blend in 12.4–18.0GHz range, Synth. Met. 161 (2011) 1522–1526.

[51] W. Shen, B.Y. Ren, S.Z. Wu, W. Wang, X.F. Zhou, Facile synthesis of rGO/SmFe5O12/CoFe2O4 ternary nanocomposites: composition control for superior broadband microwave absorption performance, Appl. Surf. Sci. 453 (2018) 464–476.

[52] T. Hou, Z. Jia, S. He, Y. Su, X. Zhang, B. Xu, X. Liu, G. Wu, Design and synthesis of NiCo/Co4S3@C hybrid material with tunable and efficient electromagnetic absorption, J. Colloid Interface Sci. 583 (2021) 321–330.

[53] J.-C. Shu, M.-S. Cao, M. Zhang, X.-X. Wang, W.-Q. Cao, X.-Y. Fang, M.-Q. Cao, Molecular patching engineering to drive energy conversion as efficient and environment-friendly cell toward wireless power transmission, Adv. Funct. Mater. 30 (2020) 1908299.

[54] M. Green, X. Chen, Recent progress of nanomaterials for microwave absorption, J. Mater. 5 (2019) 503–541.

[55] M. Cao, X. Wang, W. Cao, X. Fang, B. Wen, J. Yuan, Thermally driven transport and relaxation switching self-powered electromagnetic energy conversion, Small 14 (2018) 1800987.

[56] G. Cui, Y. Lu, W. Zhou, X. Lv, J. Hu, G. Zhang, G. Gu, Excellent microwave absorption properties derived from the synthesis of hollow Fe(3)o(4)@reduced graphite oxide (RGO) nanocomposites, Nanomaterials 9 (2019).

[57] H. Yang, M. Cao, Y. Li, H. Shi, Z. Hou, X. Fang, H. Jin, W. Wang, J. Yuan, Enhanced dielectric properties and excellent microwave absorption of SiC powders driven with NiO Nanorings, Adv. Optical Mater. 2 (2014) 214–219.

[58] X. Zhou, Z. Jia, A. Feng, K. Wang, X. Liu, L. Chen, H. Cao, G. Wu, Dependency of tunable electromagnetic wave absorption performance on morphology-controlled 3D porous carbon fabricated by biomass, Composites Commun. 21 (2020) 100404.

[59] T. Hou, Z. Jia, A. Feng, Z. Zhou, X. Liu, H. Lv, G. Wu, Hierarchical composite of biomass derived magnetic carbon framework and phytic acid doped polyanilne with prominent electromagnetic wave absorption capacity, J. Mater. Sci. Technol. 68 (2020) 61–69.

[60] C.H. Tian, Y.C. Du, P. Xu, R. Qiang, Y. Wang, D. Ding, J.L. Xue, J. Ma, H.T. Zhao, X. J. Han, Constructing uniform Core-Shell PPy@PANI composites with tunable Shell thickness toward enhancement in microwave absorption, ACS Appl. Mater. Interf. 7 (2015) 20090–20099.

[61] H.-J. Yang, W.-Q. Cao, D.-Q. Zhang, T.-J. Su, H.-L. Shi, W.-Z. Wang, J. Yuan, M.-S. Cao, NiO hierarchical Nanorings on SiC: enhancing relaxation to tune microwave absorption at elevated temperature, ACS Appl. Mater. Interf. 7 (2015) 7073–7077.

[62] M.S. Cao, W.L. Song, Z.L. Hou, B. Wen, J. Yuan, The effects of temperature and frequency on the dielectric properties, electromagnetic interference shielding and microwave-absorption of short carbon fiber/silica composites, Carbon 48 (2010) 788–796.

[63] G. Shen, B. Mei, H. Wu, H. Wei, X. Fang, Y. Xu, Microwave electromagnetic and absorption properties of N-doped ordered mesoporous carbon decorated with ferrite nanoparticles, J. Phys. Chem. C 121 (2017) 3846–3853.

[64] Y.C. Yin, X.F. Liu, X.J. Wei, R.H. Yu, J.L. Shui, Porous CNTs/co composite derived from Zeolitic Imidazolate framework: a lightweight, ultrathin, and highly efficient electromagnetic wave absorber, ACS Appl. Mater. Interf. 8 (2016) 34686–34698.

[65] D. Ding, Y. Wang, X. Li, R. Qiang, P. Xu, W. Chu, X. Han, Y. Du, Rational design of core-shell co@C microspheres for high-performance microwave absorption, Carbon 111 (2016) 722–732.

[66] H.-J. Yang, J. Yuan, Y. Li, Z.-L. Hou, H.-B. Jin, X.-Y. Fang, M.-S. Cao, Silicon carbide powders: temperature-dependent dielectric properties and enhanced microwave absorption at gigahertz range, Solid State Commun. 163 (2013) 1–6.

[67] Y. Zhang, X. Wang, M. Cao, Confinedly implanted NiFe2O4-rGO: cluster tailoring and highly tunable electromagnetic properties for selective-frequency microwave absorption, Nano Res. 11 (2018) 1426–1436.

[68] M. Zhang, H.-J. Yang, Y. Li, W.-Q. Cao, X.-Y. Fang, J. Yuan, M.-S. Cao, Cobalt doping of bismuth ferrite for matched dielectric and magnetic loss, Appl. Phys. Lett. 115 (2019) 212902.

[69] L. Yan, J. Liu, S. Zhao, B. Zhang, Z. Gao, H. Ge, Y. Chen, M. Cao, Y. Qin, Coaxial multi-interface hollow Ni-Al2O3-ZnO nanowires tailored by atomic layer deposition for selective-frequency absorptions, Nano Res. 10 (2017) 1595–1607.

[70] Z. Gao, Z. Jia, K. Wang, X. Liu, L. Bi, G. Wu, Simultaneous enhancement of recoverable energy density and efficiency of lead-free relaxor-ferroelectric BNT-based ceramics, Chem. Eng. J. 402 (2020) 125951.

[71] R. Peymanfar, S. Javanshir, Preparation and characterization of Ba0.2Sr0.2La0.6MnO3 nanoparticles and investigation of size & shape effect on microwave absorption, J. Magn. Magn. Mater 432 (2017) 444–449.

[72] P. Wang, X. Wang, L. Qiao, J. Zhang, G. Wang, B. Duan, T. Wang, F. Li, High-frequency magnetic properties and microwave absorption performance of oxidized Pr2Co17 flakes/epoxy composite in x-band, J. Magn. Magn. Mater. 468 (2018) 193–199.